PAPER

Check for updates

A new dual-ion hybrid energy storage system with energy density comparable to that of ternary lithium ion batteries†

Shenggong He,‡[a] Shaofeng Wang,‡[a] Hedong Chen,‡[a] Xianhua Hou*[a] and Zongping Shao ✪ *[bc]

Supercapacitors that store energy through dual electrochemical layer capacitance or surface faradaic redox reactions are characterized by their fast charging/discharging capability, high power densities, and long cycling lifetime. However, the low energy density of supercapacitors seriously inhibits their practical applications. Herein, a dual-ion hybrid energy storage system using expanded graphite (EG) as the anion-intercalation supercapacitor-type cathode and graphite@nano-silicon@carbon (Si/C) as the cation intercalation battery-type anode is designed for efficient energy storage. The Si/C anode, synthesized by interfacial adhesion between nanosilicon and graphite with the help of pitch, demonstrates high specific capacity, remarkable cycling stability, and enhanced rate capability. Meanwhile, the EG cathode, which stores energy based on electrochemical double layer capacitance through its unique faradaic pseudocapacitive negative anion intercalation behaviour, demonstrates high energy densities of 462.9–356.5 W h kg^{-1} at power densities of 403–7130 W kg^{-1}. The resulting Si/C//EG hybrid system delivered highly attractive energy densities of 252–222.6 W h kg^{-1} at power densities of 215–5420 W kg^{-1}, which are superior to those of conventional electrochemical double layer capacitors and lithium-ion capacitors, making the dual-ion hybrid system a new type of energy storage device capable of achieving fast and efficient energy storage.

1. Introduction

State-of-the-art lithium-ion batteries (LIBs) with the LiCoO$_2$ cathode and graphite anode have been successfully used in portable electronics for around thirty years.[1–5] Such batteries have a limited theoretical capacity of only 274 mA h g^{-1}, and currently a practical capacity of 140 mA h g^{-1} has already been reached.[6] However, the increasing demand for higher power density, safer and cheaper electrochemical energy storage systems from the fields of most sophisticated portable electronics, electrified transportation and smart grids has triggered intensive research activities in the development of novel energy storage systems which potentially deliver higher energy density than commercial LIBs.[7–9]

Considering the limited theoretical capacity of the LiCoO$_2$ cathode and graphite anode, ternary LiNi$_{1−x−y}$Co$_x$Mn$_y$O$_2$ cathodes (LNCM, with a theoretical capacity of 280 mA h g^{-1}) and Si-based anodes (Li$_{15}$Si$_4$, 3580 mA h g^{-1}) have been extensively exploited in recent years.[10–12] By applying the ternary LNCM cathode, the energy density of LIBs can reach a theoretical value of 241 W h kg^{-1}.[13] However, big concerns about the ternary lithium batteries are their poor electrochemical stability at high voltage and poor rate performance. Due to the similar cation size of Li$^+$ and Ni^{2+}, the dislocation of the Li$^+$ and Ni^{2+} may easily occur, resulting in reduced cycling stability and reversible capacity. In addition, ternary cathode materials usually show poor thermal stability, and may easily react with liquid electrolyte at high temperature leading to dramatic performance degradation. In addition, the poor lithium-ion conductivity of LNCM, which introduces large polarization resistance at high rates, accounts for poor rate performance.[14–17]

Supercapacitors, another type of extensively investigated electrochemical energy storage device distinguished by high power density and cycling stability, store energy through electrochemical double layer capacitance at the surface of both

[a]Guangdong Provincial Key Laboratory of Quantum Engineering and Quantum Materials, Guangdong Engineering Technology Research Center of Efficient Green Energy and Environment Protection Materials, Engineering Research Center of MTEES (Ministry of Education), School of Physics and Telecommunication Engineering, South China Normal University, Guangzhou 510006, China. E-mail: houxianhua@m.scnu.edu.cn

[b]Jiangsu National Synergetic Innovation Center for Advanced Materials (SICAM), State Key Laboratory of Materials-Oriented Chemical Engineering, College of Chemical Engineering, Nanjing Tech University, Nanjing, 210009, China. E-mail: Shaozp@njtech.edu.cn

[c]WA School of Mines: Minerals, Energy and Chemical Engineering (WASM-MECE), Curtin University, Perth, WA, 6845 Australia

† Electronic supplementary information (ESI) available. See DOI: 10.1039/c9ta12660k

‡ These authors contributed equally.

This journal is © The Royal Society of Chemistry 2020

J. Mater. Chem. A, 2020, **8**, 2571–2580 | 2571

electrodes.[18–20] However, such supercapacitors usually show relatively low energy density inferior to that of conventional LIBs.[21–23] By introducing pseudocapacitance into the electrodes, the energy storage performance is enhanced through surface faradaic redox reactions, and consequently the capacity can be greatly improved. Up to now, the highest energy density of supercapacitors based on pseudocapacitance has been reported to be around 100 W h kg^{-1},[24] which is however still inferior to that of conventional LIBs. Recently, supercapacitors based on a battery-like ion-intercalation mechanism have received considerable attention showing the capability of increasing energy density.[25–28] Both cation-intercalation and anion-intercalation have been reported for supercapacitors. Up to now, an energy density as high as 231.7 W h kg^{-1} has been reported,[29] which is already comparable to that of conventional LIBs with the LiCoO$_2$ cathode and graphite anode. In order to reach further improvement of energy density, new advances in the materials composition and energy storage mechanism should be exploited.

Considering the high energy density of LIBs and high power density of supercapacitors, a new type of electrochemical system called the hybrid energy storage system was proposed. In this system, one electrode (typically the cathode) stores charge by a supercapacitor behavior, while the other electrode stores energy *via* conventional LIB behavior, so that it could have the advantages of both the supercapacitor (high power density and cycling stability) and the battery (high energy density).[30–34] It is highly promising as the next-generation electrochemical storage device. Note that, due to the capacity limit of the supercapacitance electrode, the energy density of the reported devices is yet still lower than that of the conventional LIBs.[29]

For the above-mentioned energy storage devices, LIBs, supercapacitors and the hybrid system, the lithium ion plays roles in adsorption or intercalation. More recently, dual ion batteries, in which both the cation (lithium ion) and anion (PF$_6^-$) can be used for energy storage, have received considerable attention.[35–38] The theoretical energy density can be further improved. However, the lack of suitable electrodes limits the energy density of dual ion batteries to be lower than 200 W h kg^{-1}.[39,40] Taking advantage of the dual-ion battery system, a special dual-ion hybrid electrochemical device constructed using a high voltage supercapacitor-type cathode and a battery-type anode *via* a dual-ion mechanism may lead to the achievement of high energy density, power density and cycling stability. Although many attempts have been made, the reported energy density is still lower than that of conventional LIBs.[41]

Here we report a new dual-ion hybrid electrochemical system that optimizes the supercapacitor-type cathode and battery-type anode to boost energy density, achieving an ultrahigh energy density of up to 252 W kg^{-1} (under a power density of 215 W kg^{-1}), which is much superior to those of most of the available supercapacitors and dual-ion batteries, and even comparable to those of LIBs. In addition, the rate performance is obviously improved. The system maintains an energy density of 222.6 W h kg^{-1} even at a high power density of 5420 W kg^{-1}. Also, the hybrid electrochemical energy storage system

demonstrates superior cycling stability with a capacity retention of 94.6% after 1000 cycles at a 1C rate. The outstanding performance is reached by taking the use of an expanded graphite as an anion-intercalation-type pseudocapacitor cathode and a battery-type Si–graphite anode for energy storage.

2. Experimental section

2.1 Synthesis of the graphite@nano-silicon@carbon (Si/C) composite

Nanosilicon (particle size: ~50 nm) was synthesized from bulk silicon by the radio frequency induction method conducted using a plasma system (TEKNANO-15; TDU15 Kw, Canada) at elevated temperature and high rates of quenching (Scheme S1, ESI†). Typically, 1.5 g nanosilicon and 16 g artificial graphite (Jiangxi Zichen Technology Co., Ltd) were mixed in 100 mL deionized water using an ultrasonic cell crusher with a power of 300 W for 30 min. After that, 2 g of pitch binder was added. The mixture was then severely ball-milled at 1000 rpm for 2.5 h. The mixture was rapidly dried by spray drying to obtain the solid precursor powder (Si/C). The as-prepared Si/C was obtained by heat treatment at 900 °C in a nitrogen-filled atmosphere for 3 h (Scheme S2, ESI†).

2.2 Structural characterization

The materials' phase and crystal structures were obtained through characterizing the materials by transmission electron microscopy (JEM-2100HR) and powder X-ray diffraction XRD (PANalytical X'Pert PRO) at a scan rate of 10° min^{-1}. Field emission electron microscopy FESEM (ZEISS GEMINI 500) was used to observe the morphology of the materials, and micro-Raman spectroscopy (Jobin Yvon LabRam HR800) was used to identify the carbon phases in the materials. To determine the content of nanosilicon in Si/C, differential scanning calorimetry DSC and thermogravimetric analysis TGA (Netzsch Sta 409) were performed, by setting the temperature from 30 to 900 °C at a rate of 10 °C min^{-1} and under a flowing air. Nitrogen adsorption (Micromeritics ASAP-2020M) was performed to evaluate the pore size and specific surface area of the samples by the Brunauer–Emmett–Teller (BET) model.

2.3 Electrochemical measurements

The electrochemical measurements used a 2032-type coin cell in an argon-filled glove box. To perform the half-cell test, the Si/C or AC (Nanjing XFNANO Materials Tech Co., Ltd) electrode served as the working electrode, *versus* metallic lithium as the reference electrode. To prepare the electrode from Si/C, 10 wt% Super-P, 10 wt% carboxymethyl cellulose CMC (Aladdin) and 80 wt% active material were mixed using deionized water. The resulting homogeneous slurry was then spread on the surface of copper and aluminum foil, and vacuum-dried at 70 °C. The mass of the active material was kept around 1 mg cm^{-2}. The EG and AC electrodes were made by mixing 10 wt% Super-P, 10 wt% polyvinylidene fluoride and 80 wt% active material in *N*-methylpyrrolidone solution. Then the homogeneous slurry was spread on the surface of Al foil, and vacuum-dried at 70 °C. The

2572 | *J. Mater. Chem. A*, 2020, **8**, 2571–2580

This journal is © The Royal Society of Chemistry 2020

mass of the active material was kept around 2 mg cm^{-2}. The dual-ion hybrid device (Si/C//EG) was also assembled in coin cells with the Si/C anode and EG cathode, and the optimized weight ratio of the anode and cathode was 1 : 4. The electrolytic solution of the cell was 4.0 M LiPF$_6$ in ethyl-methyl carbonate (EMC, 98%) with 2.0 wt% vinylene carbonate (VC, 99.5%) as the additive. A microporous film (Celgard-2400) was used as the separator.

The galvanostatic charging and discharging tests used a Neware BTS-3S test system. The hybrid cell full device was cycled within a voltage window of 3.0 and 5.0 V, and the rate capability was evaluated using a range of current densities from 0.1 to 1.6 A g^{-1}. A Solartron 1470E/1400 potentiostat was used to obtain cyclic voltammetry (CV) curves, and also to perform the electrochemical impedance spectroscopy (EIS) tests that were carried out within a frequency range from 100 kHz to 0.01 Hz. The energy (E) and power density (P) calculation details are explained in Notes S1 and S2.†

3. Results and discussion

To improve the energy density of a hybrid dual-ion electrochemical energy storage system, the capacity of both electrodes should be maximized. It is well known that Si has much higher theoretical capacity (3580 mA h g^{-1}) for lithium storage than graphite.[42] However, due to the large volume change (∼300%) during alloying and de-alloying processes and poor electrical conductivity, bulk silicon used as the electrode material faces big challenges.[43] Instead, nanosized Si can assist in the formation of a composite with graphite to increase the capacity of the anode. Previously graphite embedded in a coating silicon nanoparticle matrix as an excellent anode for LIBs has been reported.[44] Here, a similar graphite-nanosized silicon based composite (Si/C) was prepared.

Fig. 1a and b show the SEM images of the as-prepared Si/C composite in disk morphology with particle size ranging from 10 to 20 μm. The magnified SEM image and TEM image in Fig. 1c and d show the surface of the main particles which was rough and decorated with a large amount of nanoparticles sizing around 50 nm. The nature of silicon nanoparticles with a 5 nm carbon shell is clearly observed and its crystalline spacing with 0.317 nm corresponds to the silicon crystal (Fig. 1e). Fig. 1f shows the selected area electron diffraction (SAEM) of the center of Si/C which exhibits diffraction rings and light diffraction spots. The content of carbon and silicon in the composite was found to be approximately 92.4 and 7.6 wt%, respectively, based on thermogravimetric (TG) analysis (Fig. S1, ESI†). The large weight percentage of carbon can effectively relieve the stress caused by the volume change of silicon during the charge–discharge processes.

Si/C composites were evaluated by half-cell tests against Li metal at potentials between 0.01 and 1.5 V. Fig. 2a presents the first five CV cycles of the half-cell at a scan rate of 0.1 mV s^{-1}. Two peaks located at 0.54 and 0.93 V of the first cathodic scan originated from the formation of a solid electrolyte interface (SEI) on the Si/C. The cathodic peak at 0.12 V originated from the insertion of lithium and the formation of the amorphous Li$_x$Si phase (a-Si + xLi → a-Li$_x$Si). Meanwhile, an anodic peak at 0.35 V arose due to the extraction of lithium from alloyed Li–Si (a-Li$_{x+y}$Si → a-Li$_x$Si + yLi + ye$^-$). The CV curves almost overlapped in the following four cycles, showing reversible behavior. The rate capability of the Si/C electrode was also tested at varied current densities and the results are shown in Fig. 2b. Reversible capacities of 488.8, 443.9, 389.8, 317.0, 283.0, and 270.5 mA h g^{-1} were achieved at current densities of 100, 200, 400, 800, 1000, and 1600 mA g^{-1}, respectively, indicating superior capacity and rate capability. After the current density was reset to 100 mA g^{-1}, the cell retained a capacity of 487.1 mA h g^{-1}. Galvanostatic charge and discharge curves were measured at 100 mA g^{-1} current density and are plotted in Fig. 2c. The galvanostatic curves of the Si/C electrode showed a distinct discharge voltage plateau below 0.3 V, demonstrating that lithium ions had embedded in Si/C particles to form the Li$_x$Si alloy and Li$_x$C compound. The initial discharge/charge
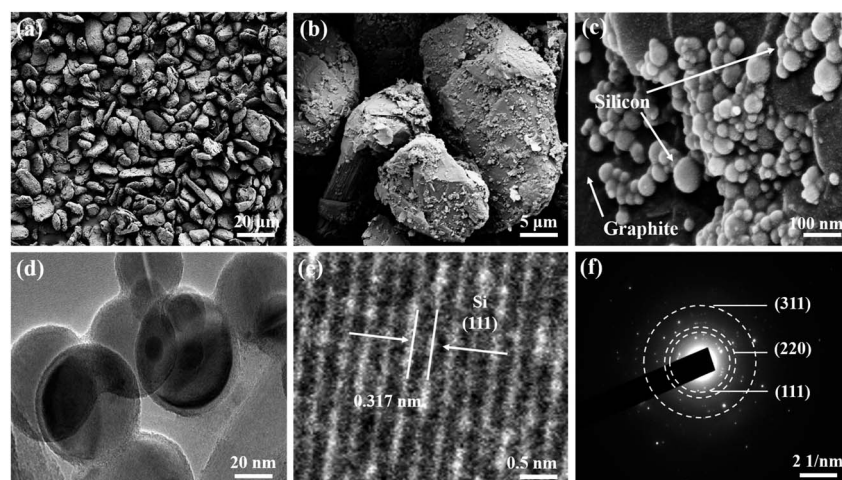

Fig. 1 (a–c) SEM images of the Si/C composite under varied magnifications; (d) TEM image, (e) HR-TEM image and (f) selected area electron diffraction patterns of the Si/C composite.
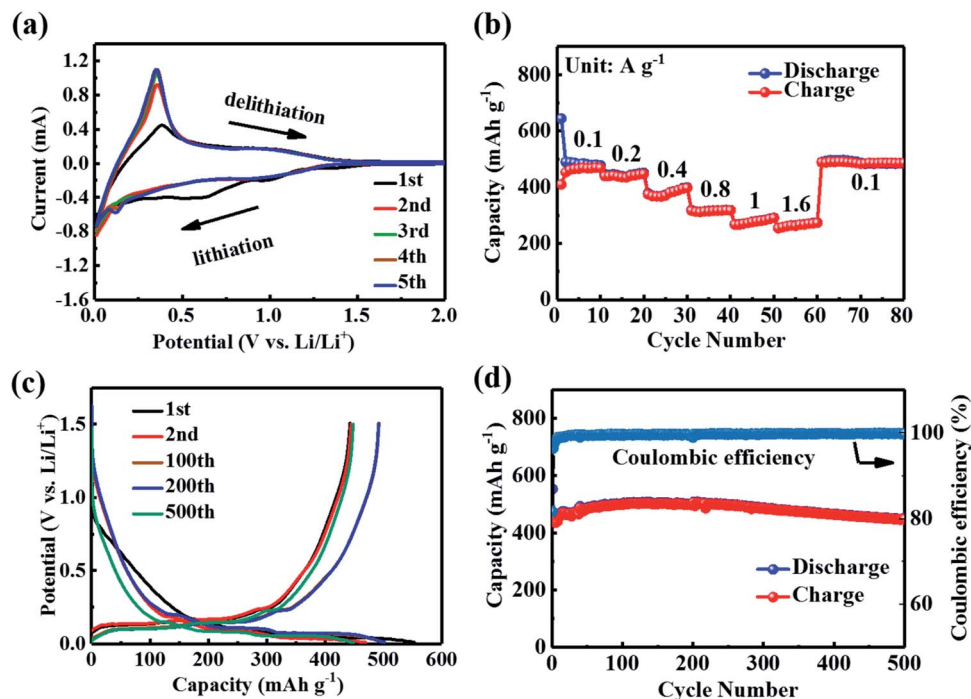
Fig. 2 (a) CV curves at a scan rate of 0.1 mV s^{-1}, (b) rate performance at varied currents, (c) charge/discharge profiles and (d) long cycling performance at 100 mA g^{-1} of the Si/C electrode.

capacities were 553 and 448 mA h g^{-1}, respectively. And the initial coulombic efficiency was 81.1%. The loss of charge capacity was due to the formation of SEI films.[46,47] The discharge capacity showed a significant increase within 200 cycles and reached a maximum value of 500 mA h g^{-1}. Such capacity increment was found to be accompanied by the formation of a polymeric gel layer, which came from the degradation of the electrolyte, over the electrode. For long cycling performance at 100 mA g^{-1} (Fig. 2d), the electrode still delivered a reversible capacity of 449.4 mA h g^{-1} after 500 cycles, implying outstanding cycling stability.

Since the energy density of a hybrid device is determined by both the capacities and the working voltage, the cathode capacity and operating voltage are also of significance. Graphite, which can store anions like PF$_6^-$ and TFSI$^-$ under high operating voltage *via* intercalation into the interlayer space,[37,38] was extensively used as the cathode for dual ion LIBs. It was demonstrated that the storage of PF$_6^-$ anions into graphite occurs through pseudocapacitive intercalation behavior instead of chemical intercalation behavior. Considering that the ion size of PF$_6^-$ (4.36 Å) is much larger than the interlayer spacing of graphite layers (3.36 Å), increasing the layer distance may benefit the PF$_6^-$ anion insertion. In this work, EG, which was prepared according to a previous report,[48] was selected as the cathode. Fig. 3a shows the SEM image of the as-prepared EG. EG displayed an interconnected sheet-like morphology and provided a moderate surface area of 90.4 m^2 g^{-1} (Fig. S2, ESI†). EG presented a diffraction peak at $2\theta = 26.6°$ referring to the (002) plane of graphite (Fig. 3b), corresponding

to an interlayer distance of 3.46 Å. The value enlarged as compared to that of crystal graphite.

The electrochemical performance of EG for PF$_6^-$ anion storage was evaluated by galvanostatic charge/discharge measurements at varied currents as shown in Fig. 3c. For comparison, activated carbon (with a surface area of 1768 m^2 g^{-1}, Fig. S2, ESI†) was also tested. Three distinct platforms (4.40–4.68, 4.68–4.82 and 4.82–5.00 V) on the charging branch and three platforms (4.97–4.74, 4.74–4.46 and 4.46–4.12 V) on the discharge branch were observed. This suggested that the intercalation and de-intercalation processes occurred *via* a stage-like mechanism, agreeing well with the previous literature reports.[49,50] The rise of current density from 100 to 1600 mA g^{-1} just caused a modest decrease in the capacity of the EG electrode from 104.1 to 76.7 mA h g^{-1}, implying enhanced electrode reaction kinetics. Note that the AC cathode delivered capacities of only 60.9 and 36.9 mA h g^{-1} at current densities of 100 and 1600 mA g^{-1} (Fig. S3a, ESI†). Fig. S3b (ESI†) shows the rate capability of the EG electrode, which was much superior to AC, exhibiting excellent reversible capability. The cycling stability of the EG electrode was also tested at a fixed current density of 100 mA g^{-1} as shown in Fig. S3c (ESI†). The electrode maintained a high capacity of 96 mA h g^{-1} after 200 cycles. The energy density of the EG electrode, calculated by the V_m (the midpoint discharge voltage obtained from the discharge curves.) and capacity, ranged from 418.1 to 488 W h kg^{-1} at power densities of 0.456–9.786 kW kg^{-1}, superior to the 109.4–235.1 W h kg^{-1} of the AC electrode at 0.378–8.971 kW kg^{-1} (Fig. S3d, and Note S1, ESI,† which explained the details of the calculations).

2574 | *J. Mater. Chem. A*, 2020, 8, 2571–2580

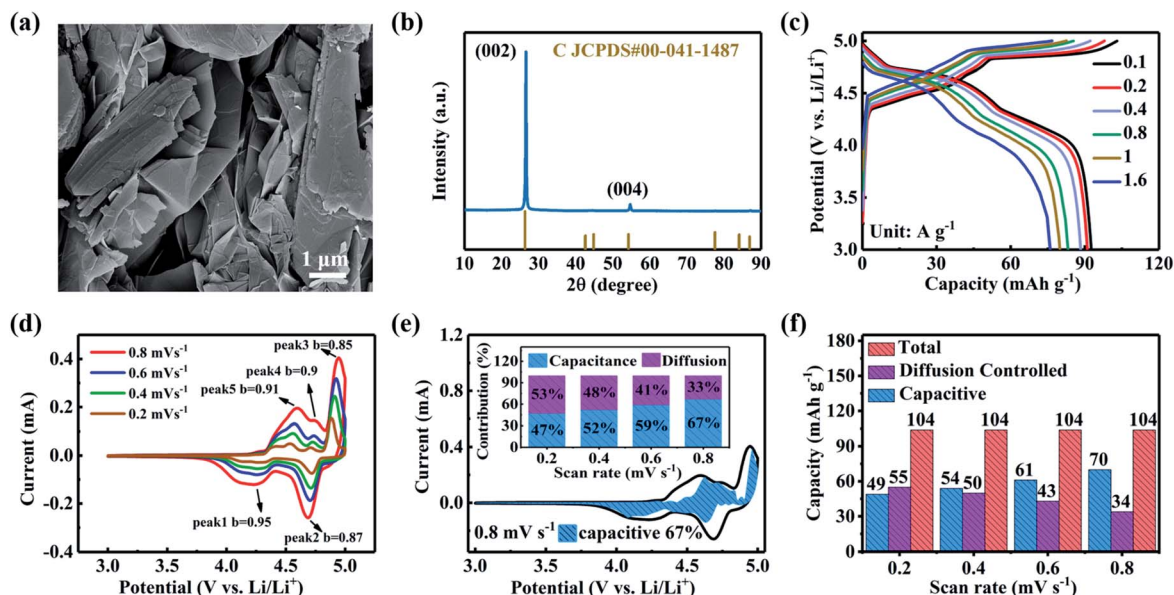This journal is © The Royal Society of Chemistry 2020

Fig. 3 (a) SEM image and (b) XRD patterns of the as-prepared EG; (c) charge/discharge profiles at varied currents rates and (d) CV curves at varied scan rates of the EG electrode; (e) CV curves with capacitive contribution (shadowed area) at 0.8 mV s⁻¹ (insert: the contribution ratio of diffusion-controlled and capacitive *versus* scan rate) and (f) capacitive, diffusion-control and total capacities for varied scan rates of the EG electrode.

To confirm the energy-storage behavior of the EG electrode for PF_6^- anion storage, cyclic voltammetry (CV) curves were measured using varied sweep rates and the results are shown in Fig. 3d and S5 (ESI†). In general, the peak current (i) could be correlated with the sweep rate (v) *via* eqn (1) and (2) as follows:[25,45]

$$i = av^b \tag{1}$$

$$\log(i) = b\log(v) + \log(a) \tag{2}$$

in which a and b were adjustable parameters. Parameter b is calculated from the plot of the curves $\log(v)$ *versus* $\log(i)$. If the b value is close to 0.5, the capacity can be dictated by diffusion in the solid-state; and if the value is close to 1.0, the electrochemical process will be more like a capacitor mechanism. In this work, the b values of the EG cathode are 0.91, 0.9, 0.85, 0.87 and 0.95, which were all close to 1.0, confirming the pseudo-capacitive behavior for the PF_6^- anion intercalation into the EG electrode. In terms of the AC electrode, the CV curves (Fig. S4, ESI†) showed a featureless rectangular shape, suggesting the electrical double layer capacitance mechanism.[51] To distinguish contributions of diffusion and capacitive behavior, eqn (3) and (4) were calculated:[25,45]

$$i = k_1 v^{1/2} + k_2 v \tag{3}$$

$$i/v^{1/2} = k_1 + k_2 v^{1/2} \tag{4}$$

$k_1 v^{1/2}$ represented the fraction of the process controlled by diffusion, and $k_2 v$ represented the contribution of capacitive behavior. The calculated results are presented in Fig. 3e. The capacitive contribution reached 47% when the sweep rate was

low (0.2 mV s⁻¹), whereas when a higher sweep rate (0.8 mV s⁻¹) was applied, the capacitive ratio increased to 67%. With the sweep rate rising, the contribution of the pseudocapacitance increased, indicating the high PF_6^- intercalation/de-intercalation capability of the EG electrode at high rates. Fig. 3f shows the calculated capacities contributed by the two mechanisms. The capacitive mechanism capacities at sweep rates of 0.2, 0.4, 0.6 and 0.8 mV s⁻¹ were 49, 54, 61 and 70 mA h g⁻¹ and the diffusion controlled capacities were 55, 50, 43 and 34 mA h g⁻¹. This evidently indicated that the behavior was pseudocapacitive in nature. Another line of evidence of the pseudocapacitive nature of PF_6^- intercalation/de-intercalation of the EG electrode was that the plateau appeared on the voltage profiles in Fig. 3c.[18]

CV curves of the lithium-based hybrid dual-ion energy storage device (Si/C//EG) were recorded within the potential window of 3.0 to 5.0 V with the results shown in Fig. 4a. Three sets of redox peaks were observed that corresponded to the intercalation/de-intercalation of ions into/from the electrode. Three reduction peaks (3.71, 4.18, and 4.55 V) and the equivalent oxidation peaks (4.37, 4.47, and 4.68 V) of the Si/C//EG cell, which were attributed to the intercalation/de-intercalation of PF_6^- anions into/from the interlayers of graphite,[17] remained visible. Notably, the CV curves retained their shape over the cycles, indicating that electrochemical reactions took place in a highly reversible manner.

The charging/discharging profiles of the Si/C//EG device at a current density of 100 mA g⁻¹ (Fig. 4b) showed three reduction peaks located at approximately 3.70, 4.15 and 4.76 V and corresponding oxidation peaks at approximately 4.40, 4.49 and 4.70 V. These results were consistent with the stage-like potentials on the CV curves. To obtain the rate capability, the
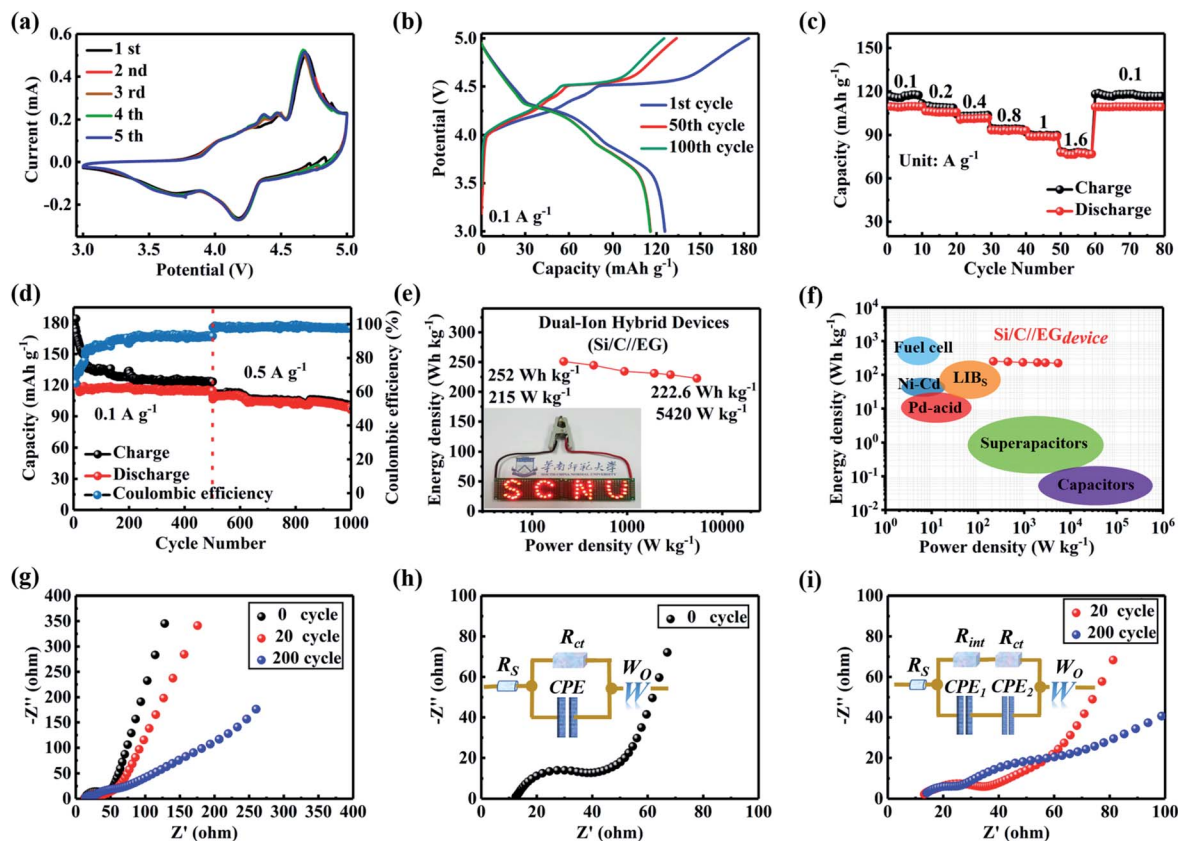
This journal is © The Royal Society of Chemistry 2020

J. Mater. Chem. A, 2020, **8**, 2571–2580 | **2575**

Fig. 4 Electrochemical performance of Si/C//EG devices. (a) CV curves of the devices at 1 mV s^{-1}. (b) Charge and discharge curves of devices in the potential window of 3.0–5.0 V at 100 mA g^{-1}. (c) Rate performance of the devices. (d) The long-term cycling stability at 100 mA g^{-1} and 500 mA g^{-1}. (e) Ragone plots (energy density *vs.* power density) of devices. Inset: photograph of 50 LED lamps lit up by one device. (f) Device-based performance of the currently available energy-storage systems. (g) Nyquist plots of the devices after 0, 20 and 200 cycles. (h) High-frequency region magnified view before cycling, and (i) after 20 and 200 cycles, and the corresponding equivalent circuit model.

hybrid cell was further tested at various current densities from 0.1 to 1.6 A g^{-1} (Fig. 4c). The cell delivered reversible discharge capacities of 109.7, 106.6, 101.3, 93.4, 89.2, and 77.9 mA h g^{-1} under 0.1, 0.2, 0.4, 0.8, 1, and 1.6 A g^{-1}, respectively. Note that, after cycling at a current density of 1.6 A g^{-1}, a discharge capacity of 109.4 mA h g^{-1} was achieved when the current was set back to 0.1 A g^{-1}.

It should be mentioned that the hybrid device suffered from high irreversible charge capacity, originating from the formation of the SEI layer,[52] leading to low coulombic efficiency during the original cycles. The device delivered a discharge capacity of 122.7 mA h g^{-1} under a current of 0.1 A g^{-1} in the beginning (Fig. 4d). The coulombic efficiency was 66.7% in the first cycle, but the value later increased to more than 90% after 100 cycles under a current density of 0.1 A g^{-1}. After cycling for 500 cycles, the current density was set to 0.5 A g^{-1}. The cell provided a discharge capacity of 96.4 mA h g^{-1} with coulombic efficiency climbing as high as 97.8%. The Ragone plots of Si/C//EG devices are presented in Fig. 4e. The energy and power densities were calculated based on the total mass of active materials in both the anode and cathode. The maximum energy density reached 252 W h kg^{-1} at a power density of 215 W kg^{-1} (the details of the calculation are given in Note S2, ESI†). The Si/

C//EG full cell maintained a high energy density of 222.6 W h kg^{-1} even at a high power density of 5420 W kg^{-1}, demonstrating remarkable energy/power delivery compared with recently reported dual graphite pseudocapacitors (energy densities of 231.7–220.2 W h kg^{-1} at power densities of 222–4409 W kg^{-1}). This enhanced performance was associated with the fact that the silicon carbon anode provided a higher capacity than the graphite anode, which was more beneficial to improve energy density. The energy/power densities of the Si/C//EG exceed those of benchmark double-ion batteries, supercapacitors, lithium-ion capacitors and pseudocapacitors as reported in the literature (Table S4, ESI†). Since the mass of active electrode materials accounted for 35–40% of the total package,[53–55] the Si/C//EG could achieve an energy density comparable to that of a commercial LIB (Fig. 4f). And the power density could also be comparable to that of supercapacitors maintaining an appropriate value.

To gain insight into capacity fading during cycling, electrochemical impedance spectroscopy (EIS) was conducted for the original cell and the cell after 20 and 200 galvanostatic cycles (Fig. 4g). The Nyquist diagram demonstrated a semicircle in the region of high-frequency and a straight line in the region of low-frequency. The high frequency region is controlled by the

electrode reaction kinetics, and the low frequency region is controlled by the diffusion of reactants or products of the electrode reaction. During the cycle, repeated intercalation/delamination of ions at the insulating layer caused a certain change in the electrode material interface. This process belongs to electrode reaction kinetics. So it appears in the high-frequency region after cycling. The internal impedance was shown through its equivalent circuit model inset of Fig. 4h and i. In this model, R_s represented the resistance of the electrolyte solution. W_o referred to the Warburg impedance arising from diffusion of ions into the electrodes. The value of R_s was quite low (12.0 Ω), suggesting low resistance in the electrolyte solution. In addition, the two semicircles that emerged in the high-frequency region after cycling corresponded to R_{ct} and R_{int} paralleled with the constant phase element (CPE), accounting for the charge transfer impedance and the contact impedance, respectively.[56] Notably, only a small increase in the impedance was seen (from 40.0 to 60.0 Ω). Thus, the decay in the capacity with cycling may not be due to the deteriorated reaction kinetics, but mainly due to a loss of Si nanospheres from the electrode, suggesting an important influence of the carbon, the binder pitch and the volume buffer on the integrity of the core–shell-like structure of Si nanospheres in the Si/C composite anode.

Multiscale characterization techniques including *ex situ* XRD, SEM and Raman spectroscopy have been carried out. As shown in Fig. 5, the Si/C electrode after the full cell charging to 5.0 V showed a significant difference in diffraction peaks, which could be attributed to the Li_xSi alloy during the charging processes, compared with the electrode material before charging (Fig. 5a). Fig. 5b and c show the morphology change of

the Si/C before and after cycling under a current density of 500 mA g^{-1}. Before cycling, the Si/C electrode showed a smooth surface. After cycling, the Si/C electrode presented huge erosion/exfoliation on the surface resulting from the alloying/de-alloying reaction causing volume changes.

For the EG electrode, there is no obvious morphology change in the electrode morphology before and after the electrochemical reaction as shown in Fig. 5d and e. Further, *ex situ* X-ray diffraction (XRD) and Raman spectroscopy had been carried out. The XRD patterns of the EG electrode at certain charge states are presented in Fig. 5f. With the charging potential reaching a value over 4.5 V (*vs.* Li/Li$^+$), the (002) peak of non-intercalated EG was replaced by two fresh peaks at 23–26° and 30–35°, assigned to the (00n) and (00n + 1) peaks of intercalated EG compounds. Moreover, the emergence of the peak (00n + 1) was a clear indication of the intercalation of PF$_6^-$ between the layers of EG. When the EG electrode was charged to higher potentials (5.0 V), the (00n) peak shifted gradually to a low angle while the (00n + 1) peak shifted to a high angle, indicating a stage-like intercalation of PF$_6^-$ (from stage 4 to stage 1 as seen in Fig. S6, and Table S5, ESI†). During discharging, the peaks (00n) and (00n + 1) started to shift gradually in an opposite manner, until the (00n + 1) peak disappeared, and the position of the non-intercalated peak was recovered.[49] Comparing these changes to the processes of charging and discharging of the EG cathode, the appearance of the same (00n) peak in the same state indicated that the change in the interlayer distance during charging/discharging took place reversibly, which was in agreement with the results of the electrochemical measurements demonstrated above. Raman spectroscopy measurements were also performed for the EG cathode, shedding light
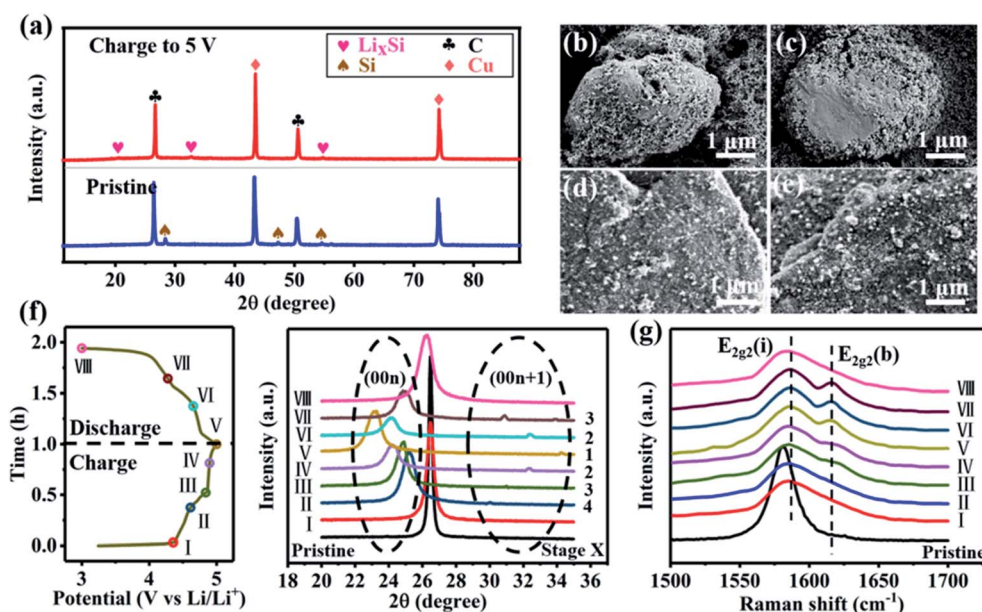

Fig. 5 (a) XRD patterns of the Si/C anode: pristine and charged to 5.0 V. (b and c) SEM images of the Si/C anode and (d and e) SEM images of the EG cathode before and after cycling. (f) The charging and discharging curves of the EG cathode at 100 mA g^{-1} and *ex situ* XRD patterns of EG, taken at various states of charging, as pointed out by the equivalent electrochemical curves. (g) *Ex situ* Raman patterns of EG, taken at various states of charging, as pointed out by the equivalent electrochemical curves.
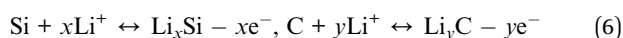
This journal is © The Royal Society of Chemistry 2020

J. Mater. Chem. A, 2020, **8**, 2571–2580 | **2577**

on the intercalation and de-intercalation of PF_6^- of the electrode (Fig. 5g). The original EG cathode displayed a well-defined G band at 1581 cm^{-1}, attributed to the E_{2g} vibration mode and the bond stretching in the sp^2 carbon.[50] In the course of charging, the G band changed into a doublet ($\sim$1584 cm^{-1} attributed to the E_{2g2}(i) mode and $\sim$1610 cm^{-1} due to the E_{2g2}(b) mode), due to the electronic effect of the intercalant species and symmetry variation of the boundary EG layer. Concurrently, the peak intensity of the E_{2g2}(b) mode increased with charging, indicating the gaining of PF_6^- anions intercalating into the EG cathode. During discharging, the two obvious peaks were still observed, which can be induced by the de-intercalation of PF_6^- anions from the interlayers of EG. With the continuous discharging of the electrode to 3.0 V, the EG returned to its symmetrical structure, showing reversible de-intercalation of the PF_6^- anion from the EG cathode.

Based on multiscale characterization test results, it could be concluded that the PF_6^- anions were intercalated/deintercalated into/from EG interlayers during charge/discharge processes and Li$^+$ had formed the Li$_x$Si alloy at the Si/C anode electrode.[57–59] Therefore, it can be inferred that the overall reaction taking place in the dual-ion hybrid devices (Si/C//EG) may be expressed in the following manner:
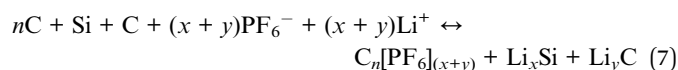
Cathode:

$$n\text{C} + (x + y)\text{PF}_6^- \leftrightarrow \text{C}_n[\text{PF}_6]_{(x+y)} + (x + y)\text{e}^- \quad (5)$$

Anode:

$$\text{Si} + x\text{Li}^+ \leftrightarrow \text{Li}_x\text{Si} - x\text{e}^-, \text{C} + y\text{Li}^+ \leftrightarrow \text{Li}_y\text{C} - y\text{e}^- \quad (6)$$

Overall:

$$n\text{C} + \text{Si} + \text{C} + (x + y)\text{PF}_6^- + (x + y)\text{Li}^+ \leftrightarrow$$
$$\text{C}_n[\text{PF}_6]_{(x+y)} + \text{Li}_x\text{Si} + \text{Li}_y\text{C} \quad (7)$$

4. Conclusion

In summary, a new dual-ion hybrid electrochemical energy storage system, which consisted of lithium ion intercalation-type anode Si/C and anion-intercalation supercapacitor-like cathode EG, was successfully designed. The Si/C//EG device exhibited energy densities of 252–222.6 W h kg^{-1} under power densities of 215 to 5240 W kg^{-1}, which were the highest for hybrid systems reported to date. The anionic charge in the EG cathode was stored/delivered by the pseudocapacitive intercalation mechanism rather than surface adsorption. These combined features of enhanced capacity, high energy density and reliable rate performance for the lithium-based dual-ion hybrid system were superior to those of commercially available supercapacitors, lithium ion capacitors and commercial lithium-ion batteries.

Conflicts of interest

There are no conflicts to declare.

References

1 V. Etacheri, R. Marom, R. Elazari, G. Salitra and D. Aurbach, Challenges in the development of advanced Li-ion batteries: a review, *Energy Environ. Sci.*, 2011, **4**(9), 3243–3262.

2 L. Li, Z. Wu, S. Yuan and X.-B. Zhang, Advances and challenges for flexible energy storage and conversion devices and systems, *Energy Environ. Sci.*, 2014, **7**(7), 2101–2122.

3 J. B. Goodenough, Evolution of Strategies for Modern Rechargeable Batteries, *Acc. Chem. Res.*, 2013, **46**(5), 1053–1061.

4 J. M. Tarascon and M. Armand, Issues and challenges facing rechargeable lithium batteries, *Nature*, 2001, **414**(6861), 359–367.

5 Y. Shi, G. Chen, F. Liu, X. Yue and Z. Chen, Resolving the Compositional and Structural Defects of Degraded LiNi$_x$Co$_y$Mn$_z$O$_2$ Particles to Directly Regenerate High-Performance Lithium-Ion Battery Cathodes, *ACS Energy Lett.*, 2018, **3**(7), 1683–1692.

6 Q. Liu, X. Su, D. Lei, Y. Qin, J. Wen, F. Guo, Y. A. Wu, Y. Rong, R. Kou, X. Xiao, F. Aguesse, J. Bareño, Y. Ren, W. Lu and Y. Li, Approaching the capacity limit of lithium cobalt oxide in lithium ion batteries *via* lanthanum and aluminium doping, *Nat. Energy*, 2018, **3**(11), 936–943.

7 B. Dunn, H. Kamath and J. M. Tarascon, Electrical Energy Storage for the Grid: A Battery of Choices, *Science*, 2011, **334**(6058), 928–935.

8 T. Placke, R. Kloepsch, S. Dühnen and M. Winter, Lithium ion, lithium metal, and alternative rechargeable battery technologies: the odyssey for high energy density, *J. Solid State Electrochem.*, 2017, **21**(7), 1939–1964.

9 X. Fan, F. Wang, X. Ji, R. Wang, T. Gao, S. Hou, J. Chen, T. Deng, X. Li, L. Chen, C. Luo, L. Wang and C. Wang, A Universal Organic Cathode for Ultrafast Lithium and Multivalent Metal Batteries, *Angew. Chem., Int. Ed.*, 2018, **57**(24), 7146–7150.

10 R. Schmuch, R. Wagner, G. Hörpel, T. Placke and M. Winter, Performance and cost of materials for lithium-based rechargeable automotive batteries, *Nat. Energy*, 2018, **3**(4), 267–278.

11 M. S. Whittingham, Lithium Batteries and Cathode Materials, *Chem. Rev.*, 2004, **104**, 4271–4301.

12 H. Chen, S. He, X. Hou, S. Wang, F. Chen, H. Qin, Y. Xia and G. Zhou, Nano-Si/C microsphere with hollow double spherical interlayer and submicron porous structure to

2578 | *J. Mater. Chem. A*, 2020, **8**, 2571–2580

This journal is © The Royal Society of Chemistry 2020

enhance performance for lithium-ion battery anode, *Electrochim. Acta*, 2019, **312**, 242–250.

13 M. S. Kim, J.-H. Ryu, Y. R. Lim, I. W. Nah, K.-R. Lee, L. A. Archer and W. Il Cho, Langmuir–Blodgett artificial solid-electrolyte interphases for practical lithium metal batteries, *Nat. Energy*, 2018, **3**(10), 889–898.

14 Z. Lu and J. R. Dahn, Can All the Lithium be Removed from T_2-$Li_{2/3}[Ni_{1/3}Mn_{2/3}]O_2$?, *J. Electrochem. Soc.*, 2001, **148**(7), A710–A715.

15 J. M. Paulsen and J. R. Dahn, O_2-Type $Li_{2/3}[Ni_{1/3}Mn_{2/3}]O_2$: A New Layered Cathode Material for Rechargeable Lithium Batteries, *J. Electrochem. Soc.*, 2000, **147**(7), 2478–2485.

16 L. Wang, J. Li, X. He, W. Pu, C. Wan and C. Jiang, Recent advances in layered $LiNi_xCo_yMn_{1-x-y}O_2$ cathode materials for lithium ion batteries, *J. Solid State Electrochem.*, 2008, **13**(8), 1157–1164.

17 J. Xu, F. Lin, M. M. Doeff and W. Tong, A review of Ni-based layered oxides for rechargeable Li-ion batteries, *J. Mater. Chem. A*, 2017, **5**(3), 874–901.

18 V. Augustyn, P. Simon and B. Dunn, Pseudocapacitive oxide materials for high-rate electrochemical energy storage, *Energy Environ. Sci.*, 2014, **7**(5), 1597–1614.

19 J. R. Miller and P. Simon, Electrochemical Capacitors for Energy Management, *Science*, 2008, **321**(5889), 651–652.

20 W.-B. Zhang, X.-J. Ma, A. Loh, X. Li, F. C. Walsh and L.-B. Kong, High Volumetric Energy Density Capacitors Based on New Electrode Material Lanthanum Nitride, *ACS Energy Lett.*, 2017, **2**(2), 336–341.

21 E. T. Mombeshora and V. O. Nyamori, A review on the use of carbon nanostructured materials in electrochemical capacitors, *Int. J. Energy Res.*, 2015, **39**(15), 1955–1980.

22 P. Simon and Y. Gogotsi, Capacitive energy storage in nanostructured carbon-electrolyte systems, *Acc. Chem. Res.*, 2013, **46**(5), 1094–1103.

23 P. G. Bruce, S. A. Freunberger, L. J. Hardwick and J. M. Tarascon, Li-O_2 and Li-S batteries with high energy storage, *Nat. Mater.*, 2011, **11**(1), 19–29.

24 T. Zhai, L. Wan, S. Sun, Q. Chen, J. Sun, Q. Xia and H. Xia, Phosphate Ion Functionalized Co_3O_4 Ultrathin Nanosheets with Greatly Improved Surface Reactivity for High Performance Pseudocapacitors, *Adv. Mater.*, 2017, **29**(7), 1604167.

25 T. Brezesinski, J. Wang, S. H. Tolbert and B. Dunn, Ordered mesoporous alpha-MoO_3 with iso-oriented nanocrystalline walls for thin-film pseudocapacitors, *Nat. Mater.*, 2010, **9**(2), 146–151.

26 H. T. Sun, L. Mei, J. F. Liang, Z. P. Zhao, C. Lee, H. L. Fei, M. N. Ding, J. Lau, M. F. Li, C. Wang, X. Xu, G. L. Hao, B. Papandrea, I. Shakir, B. Dunn, Y. Huang and X. F. Duan, Three-dimensional holey-graphene/niobia composite architectures for ultrahigh-rate energy storage, *Science*, 2017, **356**(6338), 599–604.

27 M. R. Lukatskaya, O. Mashtalir, C. E. Ren, Y. Dall'Agnese, P. Rozier, P. L. Taberna, M. Naguib, P. Simon, M. W. Barsoum and Y. Gogotsi, Cation Intercalation and High Volumetric Capacitance of Two-Dimensional Titanium Carbide, *Science*, 2013, **341**(6153), 1502–1505.

28 K. Shen, J. Ding and S. Yang, 3D Printing Quasi-Solid-State Asymmetric Micro-Supercapacitors with Ultrahigh Areal Energy Density, *Adv. Energy Mater.*, 2018, **8**(20), 1800408.

29 G. Wang, S. Oswald, M. Loffler, K. Mullen and X. Feng, Beyond Activated Carbon: Graphite-Cathode-Derived Li-Ion Pseudocapacitors with High Energy and High Power Densities, *Adv. Mater.*, 2019, **31**(14), e1807712.

30 G. G. Amatucci, F. Badway, A. Du Pasquier and T. Zheng, An Asymmetric Hybrid Nonaqueous Energy Storage Cell, *J. Electrochem. Soc.*, 2001, **148**(8), A930–A939.

31 P. Jezowski, O. Crosnier, E. Deunf, P. Poizot, F. Beguin and T. Brousse, Safe and recyclable lithium-ion capacitors using sacrificial organic lithium salt, *Nat. Mater.*, 2018, **17**(2), 167–173.

32 F. Sun, X. Liu, H. B. Wu, L. Wang, J. Gao, H. Li and Y. Lu, In Situ High-Level Nitrogen Doping into Carbon Nanospheres and Boosting of Capacitive Charge Storage in Both Anode and Cathode for a High-Energy 4.5 V Full-Carbon Lithium-Ion Capacitor, *Nano Lett.*, 2018, **18**(6), 3368–3376.

33 V. Khomenko, E. Raymundo-Piñero and F. Béguin, High-energy density graphite/AC capacitor in organic electrolyte, *J. Power Sources*, 2008, **177**(2), 643–651.

34 N. Kurra, M. Alhabeb, K. Maleski, C.-H. Wang, H. N. Alshareef and Y. Gogotsi, Bistacked Titanium Carbide (MXene) Anodes for Hybrid Sodium-Ion Capacitors, *ACS Energy Lett.*, 2018, **3**(9), 2094–2100.

35 J. A. Seel and J. R. Dahn, Electrochemical Intercalation of PF_6 into Graphite, *J. Electrochem. Soc.*, 2000, **147**(3), 892–898.

36 J. A. Read, A. V. Cresce, M. H. Ervin and K. Xu, Dual-graphite chemistry enabled by a high voltage electrolyte, *Energy Environ. Sci.*, 2014, **7**(2), 617–620.

37 M. Yoshio, H. Nakamura and H. Y. Wang, Novel Megalo-Capacitance Capacitor Based on Graphitic Carbon Cathode, *Electrochem. Solid-State Lett.*, 2006, **9**(12), A561–A563.

38 N. Gunawardhana, G.-J. Park, N. Dimov, A. K. Thapa, H. Nakamura, H. Wang, T. Ishihara and M. Yoshio, Constructing a novel and safer energy storing system using a graphite cathode and a MoO_3 anode, *J. Power Sources*, 2011, **196**(18), 7886–7890.

39 M. C. Lin, M. Gong, B. Lu, Y. Wu, D. Y. Wang, M. Guan, M. Angell, C. Chen, J. Yang, B. J. Hwang and H. Dai, An ultrafast rechargeable aluminium-ion battery, *Nature*, 2015, **520**(7547), 325–328.

40 X. Zhou, Q. Liu, C. Jiang, B. Ji, X. Ji, Y. Tang and H. M. Cheng, Beyond Conventional Batteries: Strategies towards Low-Cost Dual-Ion Batteries with High Performance, *Angew. Chem., Int. Ed.*, 2019, **58**, 2–33.

41 T. Placke, A. Heckmann, R. Schmuch, P. Meister, K. Beltrop and M. Winter, Perspective on Performance, Cost, and Technical Challenges for Practical Dual-Ion Batteries, *Joule*, 2018, **2**(12), 2528–2550.

42 J. Lee, J. Moon, S. A. Han, J. Kim, V. Malgras, Y. U. Heo, H. Kim, S. M. Lee, H. K. Liu, S. X. Dou, Y. Yamauchi, M. S. Park and J. H. Kim, Everlasting Living and Breathing Gyroid 3D Network in $Si@SiO_x/C$ Nanoarchitecture for Lithium Ion Battery, *ACS Nano*, 2019, **13**(8), 9607–9619.

This journal is © The Royal Society of Chemistry 2020

J. Mater. Chem. A, 2020, **8**, 2571–2580 | **2579**

43 M. T. McDowell, S. W. Lee, W. D. Nix and Y. Cui, 25th anniversary article: understanding the lithiation of silicon and other alloying anodes for lithium-ion batteries, *Adv. Mater.*, 2013, **25**(36), 4966–4985.

44 H. Chen, X. Hou, F. Chen, S. Wang, B. Wu, Q. Ru, H. Qin and Y. Xia, Milled flake graphite/plasma nano-silicon@carbon composite with void sandwich structure for high performance as lithium ion battery anode at high temperature, *Carbon*, 2018, **130**, 433–440.

45 V. Augustyn, J. Come, M. A. Lowe, J. W. Kim, P. L. Taberna, S. H. Tolbert, H. D. Abruna, P. Simon and B. Dunn, High-rate electrochemical energy storage through Li^+ intercalation pseudocapacitance, *Nat. Mater.*, 2013, **12**(6), 518–522.

46 F. M. Hassan, R. Batmaz, J. Li, X. Wang, X. Xiao, A. Yu and Z. Chen, Evidence of covalent synergy in silicon-sulfur-graphene yielding highly efficient and long-life lithium-ion batteries, *Nat. Commun.*, 2015, **6**, 8597.

47 J. Chun, S. An and J. Lee, Highly mesoporous silicon derived from waste iron slag for high performance lithium ion battery anodes, *J. Mater. Chem. A*, 2015, **3**(43), 21899–21906.

48 J. Yan, Z. Fan, T. Wei, W. Qian, M. Zhang and F. Wei, Preparation of exfoliated graphite containing manganese oxides with high electrochemical capacitance by microwave irradiation, *Carbon*, 2009, **47**(14), 3371–3374.

49 J. A. Read, In-Situ Studies on the Electrochemical Intercalation of Hexafluorophosphate Anion in Graphite with Selective Cointercalation of Solvent, *J. Phys. Chem. C*, 2015, **119**(16), 8438–8446.

50 L. J. Hardwick, M. Hahn, P. Ruch, M. Holzapfel, W. Scheifele, H. Buqa, F. Krumeich, P. Novák and R. Kötz, An *in situ* Raman study of the intercalation of supercapacitor-type electrolyte into microcrystalline graphite, *Electrochim. Acta*, 2006, **52**(2), 675–680.

51 P. Simon and Y. Gogotsi, Materials for electrochemical capacitors, *Nat. Mater.*, 2008, **7**, 845–854.

52 X. Li, M. Gu, S. Hu, R. Kennard, P. Yan, X. Chen, C. Wang, M. J. Sailor, J. G. Zhang and J. Liu, Mesoporous silicon sponge as an anti-pulverization structure for high-performance lithium-ion battery anodes, *Nat. Commun.*, 2014, **5**, 4105.

53 M. Yang, Y. Zhong, J. Ren, X. Zhou, J. Wei and Z. Zhou, Fabrication of High-Power Li-Ion Hybrid Supercapacitors by Enhancing the Exterior Surface Charge Storage, *Adv. Energy Mater.*, 2015, **5**(17), 1500550.

54 F. Zhang, T. Zhang, X. Yang, L. Zhang, K. Leng, Y. Huang and Y. Chen, A high-performance supercapacitor-battery hybrid energy storage device based on graphene-enhanced electrode materials with ultrahigh energy density, *Energy Environ. Sci.*, 2013, **6**(5), 1623–1632.

55 J. J. Ren, L. W. Su, X. Qin, M. Yang, J. P. Wei, Z. Zhou and P. W. Shen, Pre-lithiated graphene nanosheets as negative electrode materials for Li-ion capacitors with high power and energy density, *J. Power Sources*, 2014, **264**, 108–113.

56 Y. Zhu, Y. Xu, Y. Liu, C. Luo and C. Wang, Comparison of electrochemical performances of olivine $NaFePO_4$ in sodium-ion batteries and olivine $LiFePO_4$ in lithium-ion batteries, *Nanoscale*, 2013, **5**(2), 780–787.

57 M. D. Slater, D. Kim, E. Lee and C. S. Johnson, Sodium-Ion Batteries, *Adv. Funct. Mater.*, 2013, **23**(8), 947–958.

58 Q. Xu, J.-Y. Li, J.-K. Sun, Y.-X. Yin, L.-J. Wan and Y.-G. Guo, Watermelon-Inspired Si/C Microspheres with Hierarchical Buffer Structures for Densely Compacted Lithium-Ion Battery Anodes, *Adv. Energy Mater.*, 2017, **7**(3), 1601481.

59 Y. Wen, K. He, Y. Zhu, F. Han, Y. Xu, I. Matsuda, Y. Ishii, J. Cumings and C. Wang, Expanded graphite as superior anode for sodium-ion batteries, *Nat. Commun.*, 2014, **5**, 4033.